

Research Article

Functionality of TERGO Powders during the Synthesis of PANI-Based Composites for Electrical Devices

M. A. Domínguez-Crespo ¹, A. B. López-Oyama ^{1,2}, A. M. Torres-Huerta ²,
A. R. Hernández-Basilio,¹ D. Palma-Ramírez,¹ J. A. Lois-Correa,¹ and D. S. García-Zaleta ³

¹Instituto Politécnico Nacional, CICATA-Altamira, IPN, Km 14.5 Carretera Tampico-Puerto Industrial Altamira, 89600 Altamira, Tamaulipas, Mexico

²CONACyT-Instituto Politécnico Nacional, CICATA, Unidad Altamira, Km 14.5 Carr. Tampico-Puerto. Industrial Altamira, Altamira, Tamaulipas 89600, Mexico

³Universidad Juárez Autónoma de Tabasco, División Académica Multidisciplinaria de Jalpa de Méndez, Carr. Estatal Libre VHS-COM, Km. 27+000 s/n Ranch. Ribera Alta, Jalpa de Méndez, Tabasco 86205, Mexico

Correspondence should be addressed to M. A. Domínguez-Crespo; adcrespo2000@yahoo.com.mx

Received 19 May 2018; Revised 13 August 2018; Accepted 3 September 2018; Published 29 January 2019

Academic Editor: Bhanu P. Singh

Copyright © 2019 M. A. Domínguez-Crespo et al. This is an open access article distributed under the Creative Commons Attribution License, which permits unrestricted use, distribution, and reproduction in any medium, provided the original work is properly cited.

In this work, hybrid composites were prepared using polyaniline (PANI) and electrochemically reduced graphene oxide (ERGO) by in situ polymerization. ERGO powders were obtained by a two-way route, Hummer's method, and one-step potential (-2 V) followed by annealing process at 400°C (TERGO powders): different quantities of TERGO fine particles (10, 20, and 30 wt%) were added to the in situ PANI polymerization in order to produce the hybrid composites. The morphology and structure of the PANI/TERGO compounds were characterized by Raman spectroscopy, ultraviolet-visible spectroscopy (UV-Vis), X-ray diffraction (XRD), Fourier transform infrared (FT-IR) spectroscopy, scanning electron microscopy (SEM), and transmission electron microscopy (TEM). Thermal treatment of ERGO powders pointed out high-defect surfaces with a wrinkle-type morphology (I_D/I_G ratio ~ 0.90). The emeraldine phase of PANI was obtained with a maximum value of 61%, which decreases with the amount of TERGO powders. It is also seen that composites displayed a combined morphology between PANI matrix and TERGO powders, confirming a physical interaction between both morphologies. The amount of TERGO particles into the polymeric matrix also modifies the sample microstructure from a semispherical shape to extend sheets, where PANI is sandwiched between TERGO layers. Electrical conductivity of composites slightly increases independent of the TERGO amount (30 S/m and 39 S/m) due to the rough TERGO surface that conditioned the homogeneous nucleation of a large amount of polymer (PANI) reducing the area to move the electrical charge.

1. Introduction

Since the discovery of intrinsically conducting polymers (ICPs), it has received a great interest due to its wide use as supercapacitors, fabrication of electromagnetic interference shield, electrostatic discharged materials, sensors, batteries, and barrier coatings [1–7]. Conducting properties can be achieved by reduction of the neutral state. One of these conducting polymers is polyaniline (PANI), which can be protonated (doped) or deprotonated (undoped) after simple acid or base treatment.

Chemical oxidative polymerization (also known as electrochemical polymerization) in acid media is the most recommended process to increase the electrical conductivity [4, 8–10]. PANI can form $\pi - \pi$ interactions; thereby, it has been combined with metal oxides and carbon-based materials (carbon nanotubes, fullerene, and graphene) to be used as electrode materials, gas sensors, or electronic nose, artificial muscles [11–14]. From these, the addition of graphene has been reported to provide high electrical and thermal conductivity, as well as high surface area, good cycling stability, and large capacitance values [2, 15, 16]. Recently, PANI

has been used as a special class of polymer for the production of flexible thermoelectric devices. Inorganic materials are classic thermoelectric materials, but they are unsuitable for use in low-temperature flexible devices [17]. Thermoelectric devices are used for direct conversion of heat electricity and play an important role in the development of sustainable energy-efficient technologies.

The thermoelectric yielding of a material is defined by the figure of merit (ZT); $ZT = \sigma\alpha^2/\kappa$ where σ is the electrical conductivity, α is the seebeck coefficient, and κ is the thermal conductivity of the material [18–20]. PANI has very poor thermoelectric response; however, its flexibility and low-cost features have increased the demand, based on the fact that the electronic conductivity depends on the oxidation level, molecular arrangement interchain separation degree of crystallinity, and doping. This last item is essential to increased electronic conductivity and Seebeck coefficient [17, 21–24]. For this reason, different strategies for preparing nanocomposites of inorganic material-conducting polymers to be used as flexible devices with high performance are highly demanded. PANI/graphene and poly (3,4 ethylenedioxythiophene: polystyrene sulfonate (PEDOT:PSS)/graphene have been reported as nanocomposite materials to enhance electrical conductivity and flexibility for thermoelectrical applications, although the correct way and interaction pathway to obtain novel composites of IPCs/graphene are still far to understand.

In this work, PANI/TERGO hybrid composites were prepared by in situ polymerization in order to determine the interaction type, effect of TERGO amount, and morphology on the electrical performance.

The used strategy was to carry out in situ polymerization of aniline monomer and add different quantities of TERGO powders (10, 20, and 30 wt%), which were in turn prepared by a two-way route, Hummer's method, and one step potential (-2 V) followed by annealing process at 400°C . The morphology and structure of the PANI/TERGO composites were characterized by Raman spectroscopy, ultraviolet-visible spectroscopy (UV-Vis), X-ray diffraction (XRD), Fourier transform infrared (FT-IR) spectroscopy, scanning electron microscopy (SEM), and transmission electron microscopy (TEM). The electrical resistivity in the composite was determined by four-point resistivity.

2. Experimental Section

2.1. Materials and Modified Hummer's Method. Graphite (average mesh of $20\ \mu\text{m}$, 99.99% purity), NaNO_3 , ethanol (99.5% purity), cyclohexanone (99.8% purity), chlorobenzene (99.5% purity), and H_2SO_4 were acquired from Sigma-Aldrich reagents. HNO_3 , chloroform, KMnO_4 , H_2O_2 (30%), and HCl were obtained from Fermont analytical reagents. GO was synthesized from graphite powder according to the modified Hummers' method [25]. 5 g of graphite and sodium nitrate (2.5 g) were put into 115 mL of concentrated H_2SO_4 in a cooling bath to keep a constant temperature of 5°C for 5 min. Thereafter, the mixture was stirred continuously in the bath for 2 hours meanwhile 15 g of KMnO_4 was slowly

added to prevent a sudden temperature rise. Eventually, the reaction temperature got close to 35°C and was maintained under stirring for 30 minutes. Deionized water (138 mL) was added up to reach a temperature of 98°C , and the system was kept under stirring for 30 minutes. Then, the reaction was terminated by adding deionized water (420 mL) and a gradual addition of hydrogen peroxide, 50 mL (10% (v/v)), maintaining a constant temperature of 40°C .

The solution was kept in air overnight to separate the residual medium, and the precipitate was collected for further characterization. The precipitate was collected under vacuum using a Millipore filter ($0.22\ \mu\text{m}$) and washed several times with 5% HCl (v/v); afterwards, the solid was dried at 60°C for 12 hours.

2.2. Electrochemical Reduction of GO. A typical two-cell configuration connection to a BK precision 1746B DC power supply was used to reduce electrochemically GO using 304 L austenitic stainless steel plates ($30 \times 30 \times 2\ \text{mm}$) as electrodes. A homogenous H_2SO_4 solution (30% (v/v)) was prepared with GO powders by stirring the solution for 30 min. The applied potential was of 2 V for 10 minutes.

The ERGO samples were annealed at 400°C (1 h) to evaluate the effect of the sintering temperature on the oxygen-containing groups unattached from the graphene surface and weight loss.

2.3. Chemical and Structural Characterization. PANI/TERGO composites were uniaxially compacted at 8 MPa to obtain pellets of 15.0 mm in diameter and 1.0 mm in thickness. The functional organic groups forming hybrid composites, at each experimental condition, were followed by means of FT-IR spectra using a PerkinElmer Spectrum One series 51394 infrared spectrophotometer equipped with attenuated total reflection. The samples were recorded from $4000\text{--}400\ \text{cm}^{-1}$. The chemical composition was recorded with a Renishaw inVia microscope-based Raman spectrometer. The spectra were collected using an excitation wavelength of 514 nm (2.41 eV). The measurements were performed at 0.5 mW avoiding the effect of laser heating. UV-Vis spectra were acquired using a Cary 5000 spectrophotometer, Agilent Technologies UV-Vis NIR, in the wavelength of $200\text{--}1000\ \text{nm}$ using methanol (0.1 mg/3 mL EtOH) as dissolution medium. Surface morphology of the synthesized composites was evaluated by scanning electron microscope (FEI, Nova NanoSEM 630 FESEM) using 5 kV of accelerating voltage. The structural observation of the samples was conducted by high-resolution transmission electron microscopy (FEI, Talos F200X). The phase composition of the samples was identified by X-ray diffraction (XRD) (PANalytical X'Pert Pro MPD) with $\text{CuK}\alpha$ radiation ($\lambda = 0.15406\ \text{nm}$). The data were collected between scattering angles of $5\text{--}90^\circ$ and at a scan rate of $2^\circ\cdot\text{min}^{-1}$.

3. Results and Discussion

3.1. Characterization of TERGO Powders

3.1.1. Raman Spectroscopy. Raman spectroscopy was used to evaluate the sp^2 bonding allotropes of carbon and the D/G

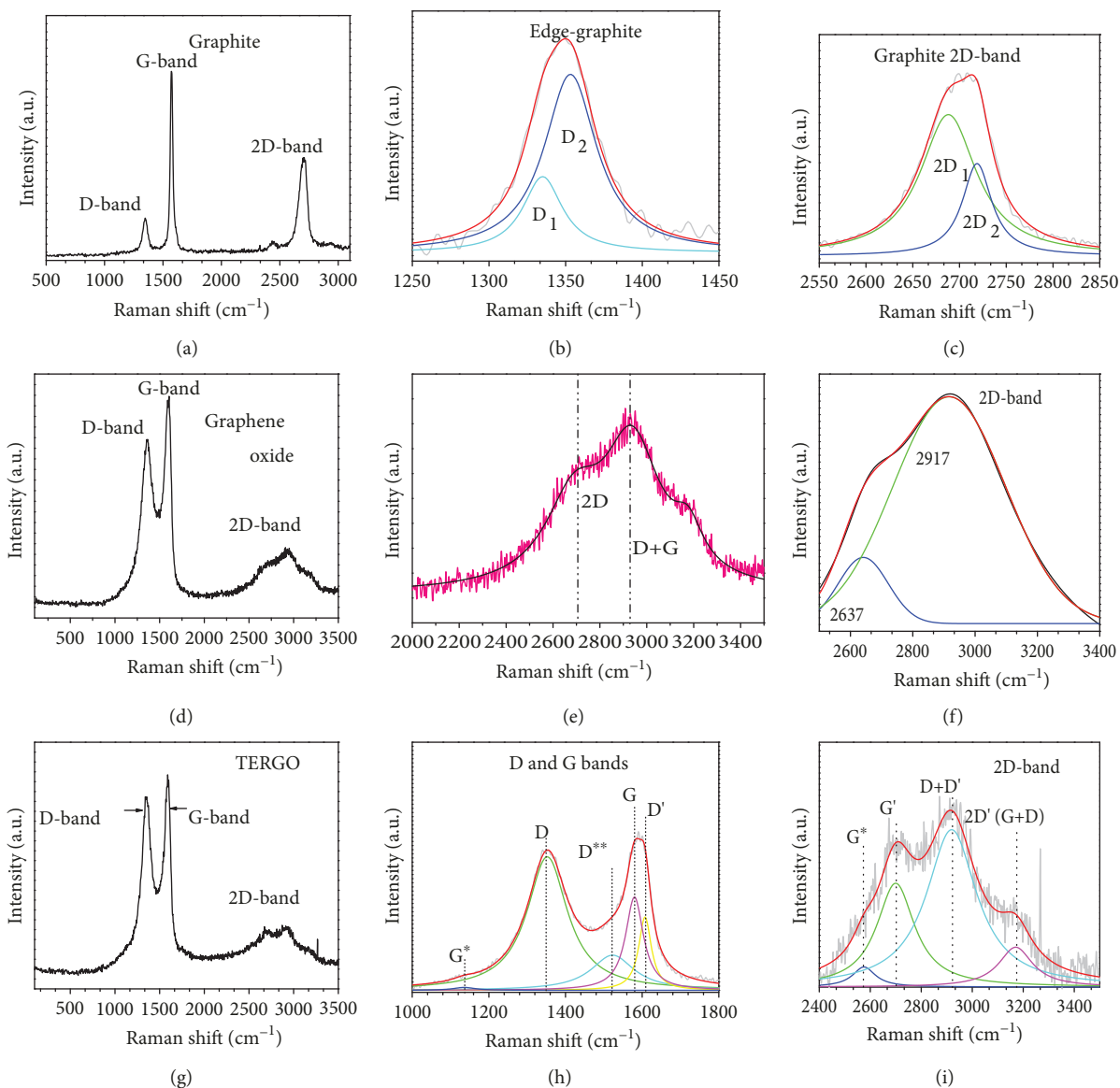


FIGURE 1: Comparison of the Raman spectra of (a–c) graphite, (d–f) GO, and (g–i) TERGO with their corresponding deconvolution.

ratio. A direct correlation between the D/G ratio and the degree of formed defects in the graphene structure has been stated; even it can be calculated in each step from graphite-GO-ERGO-TERGO.

Comparison of the Raman spectra of graphite, GO, and TERGO samples is shown in Figures 1(a)–1(i). Graphite shows the in-plane vibrations of D, G, and 2D bands at 1350 cm^{-1} , 1572 cm^{-1} , and 2700 cm^{-1} , respectively (Figures 1(a)–1(c)). D and 2D bands are assigned to the active defects of graphite [26], whereas the G band belongs to the doubly degenerate E_{2g} mode at the Brillouin zone center [27]. The integrated intensity ratio of the D and G bands (I_D/I_G ratio) was about 0.22. As it is known, the graphite structure contains pure sp^2 bonds where each carbon atom is bonded with other atoms in the hexagonal ring via σ bonds. It also has delocalized π bindings that extend throughout the entire plane. Both

sp^2 and delocalized π bonds facilitate the free movement of π electrons [28]. As a consequence, oxidation of graphite to obtain graphene oxide is associated with the covalent grafting of oxygen functional groups [29]. Raman spectrum of conversion of sp^2 -hybridized to sp^3 -hybridized atoms by graphite oxidation is shown in Figures 1(d)–1(f). The reduction in the sp^2 hybridization (σ bonds) was detected with the diminishing of G band intensity, whereas the generate defects can be correlated with the increment of the intensity of the D band [30].

Generally, the appearance of a sharp single peak (Lorentzian) at around 2700 cm^{-1} is indicative of having a single-layer graphene [31]. However, during graphite-GO transformation, the 2D peak becomes broader and splits into two peaks, the 2D and D+G bands at 2637 cm^{-1} and 2917 cm^{-1} , respectively [32–34]. In this case, the I_D/I_G ratio was found to be 0.77.

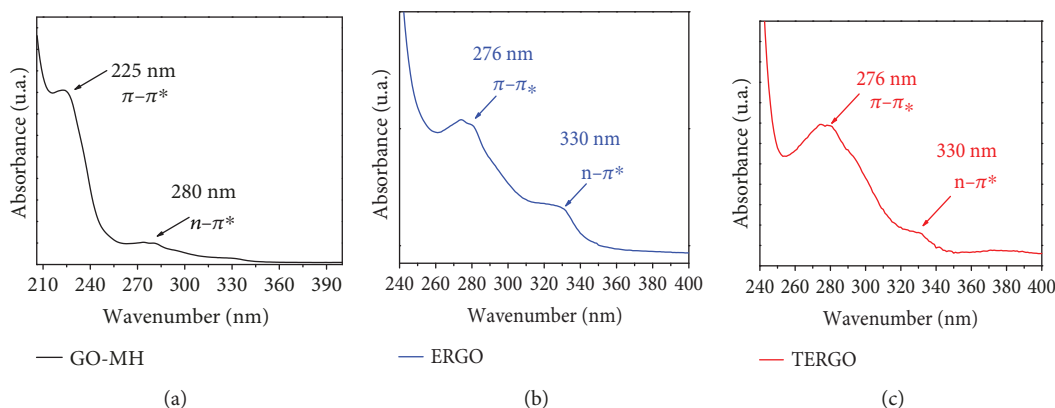


FIGURE 2: UV-Vis spectra to observe transitions from the ground state of (a) GO, (b) ERGO, and (c) TERGO.

After electrochemical reduction of GO, the ERGO powders were thermally treated to complete the reduction process at 400°C and the Raman response of these samples is shown in Figures 1(g)–1(i). Spectra deconvolution of D and G bands fitted with four bands centered at 1137 cm^{-1} , 1350 cm^{-1} , 1521 cm^{-1} , 1580 cm^{-1} , and 1609 cm^{-1} . The second and fourth peaks are associated with the conventional D and G bands, whereas the first (D') and third (D**) band peaks have been reported as amorphous disordered carbon [35, 36]. The deconvolution of 2D bands showed multiple bands at 2572 cm^{-1} , 2702 cm^{-1} , 2925 cm^{-1} , and 3174 cm^{-1} . The bands at 2572 cm^{-1} and 2702 cm^{-1} correspond to the G* and 2D (G') bands, whereas that at 2925 cm^{-1} is observed as the corresponding band of the D + D' mode or D + G mode and finally, the 3174 cm^{-1} band is commonly assigned to the 2D' and G + D' bands. Raman spectra and their fittings indicated that the TERGO samples present high-defect surfaces after the reduction process. For TERGO specimens, the I_D/I_G ratio was of 0.90 confirming the elimination of oxygen groups that generates some defects in the structure.

3.1.2. Ultraviolet-Visible Spectroscopy. Transitions from the ground to the excited states of GO, ERGO, and TERGO samples are shown in Figures 2(a)–2(c). The band at 225 nm corresponds to the $\pi - \pi^*$ transitions of the C=C bonds whereas at 280 nm, it can be seen that the $n - \pi^*$ transition correlates with the C=O bonds [37–39]. After the reduction of GO-ERGO and ERGO-TERGO, the bands shifted to higher wavenumbers from 225 to ~276 and from 280 to ~276 nm. This feature is a consequence of the reduction of π electrons. It is evident that electrochemical and thermal methods guarantee the reduction of oxide groups inducing transitions shifting the bands to higher wavenumbers [40].

3.1.3. Fourier Transform Infrared (FT-IR) Spectroscopy. FT-IR spectroscopy was used to monitor chemical changes during oxidation or reduction of functional groups. Figure 3(a) shows FT-IR spectrum of GO and consists mainly of 1715 cm^{-1} (C=O at the stretching edges), 1572 cm^{-1} (aromatic C=C bonds that were not functionalized), 1220 cm^{-1} (epoxy group C-O-H), and 1053 cm^{-1} (C-O groups) [41, 42]. After electrochemical reduction of GO (Figure 3(b)), the C=O band stays at the same position, while the C=C band

shifts to a higher wavenumber suggesting a weakening of the aromatic ring due to the $\pi - \pi$ stacking. Previous reports indicated an important enhancement of the $\pi - \pi$ stacking only after applying 20 V or 25 V during an electrochemical reduction of GO [43]. Another characteristic derived from the reduction observed is the decrease in intensity of the epoxy group C-O-H and C-O groups attached to the edges. ERGO spectra suggest that the electrochemical treatment did not remove all the oxygen-containing functional groups to produce fully reduced graphene. On the other hand, when ERGO was thermally treated (TERGO), the only feature observed in the spectra of Figure 3(c) was the shifting of the C=C band to a lower wavenumber. Thus, the annealing process (400°C) improved the $\pi - \pi$ stacking promoting strong TERGO interactions [44, 45] (see supplementary material (available here)).

3.1.4. X-Ray Diffraction (XRD). X-ray diffraction patterns of graphite, GO, and TERGO were evaluated to analyze structural changes, and the results are shown in Figure 4. Graphite powders show the typical (002) Bragg reflection of the plane of graphite at 26.71° (interlayer spacing of 3.4 Å) and the high-order (004) plane (54.85°) that corresponds to the polystyrene layers [46, 47]. After Hummer's method, the XRD pattern of GO shows a stretch signal of the (001) plane at 12.5° related to the exfoliation with interlayer spacing of about 7.8 Å [48]. The increase of interlayer spacing is mainly due to the introduction of different functional oxide groups between graphite layers [49]. Another specific reflection is the small one observed at 42.5° corresponding to the (100) plane [50].

Electrochemical reduction and thermal treatment applied to the samples provoked the destruction of the regular layer stacking of GO and are responsible of the disappearance of the (001) plane [50]. Additionally, the TERGO sample displays a new diffraction peak at 24.5° (interlayer space of 3.62 Å), which confirms a poor ordering in the stacking direction [51, 52].

3.1.5. Morphological and Microstructural Characterization. The surface morphology of the graphite, GO, ERGO, and TERGO structures is shown in Figure 5. Graphite micrographs display an enlarged surface with a flake shape, which

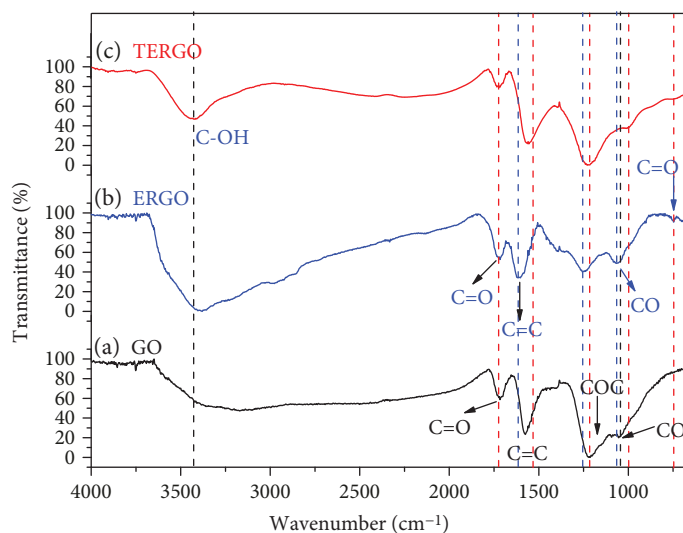


FIGURE 3: FT-IR spectra of (a) GO, (b) ERGO, and (c) TERGO.

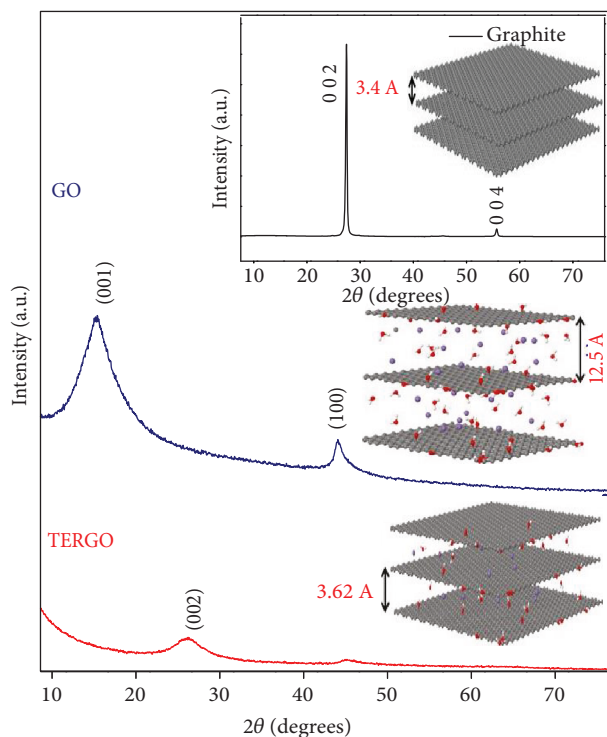


FIGURE 4: XRD patterns of Graphite, GO and TERGO powders.

is characteristic of this material (Figure 5(a)) [53]. These flakes are strongly modified during the GO production. Figure 5(b) shows crumpled- and wrinkled-layer morphologies of GO where it is possible to observe the edges of individual sheets [54]. On the other hand, Figure 5(c) displays a creased and disintegrated morphology of TERGO with finer and more defined sheets that were randomly aggregated [55]. Combination of the reduction processes produced the restoration of the hexagonal red providing a more defined sheet separation (see supplementary material). TERGO structures presented highly disordered surface containing a

wrinkled-type shape which were in turn formed by layers folding or twisting provoking deviation of the sp^2 planar character [56]. It is well stated that wrinkle and ripple morphologies depend on physical dimensions, topology, and assembling, i.e., wrinkles and ripples occur nominally on a two-dimensional plane, where wrinkles have a high aspect ratio with a thickness between 1 and 10 nm, height below 15 nm, and length above 100 nm (aspect ratio > 10); ripples are more isotropic (aspect ratio ≈ 1) valleys and peaks with a feature size below 10 nm [57]. Thus, TERGO samples showed a morphology classified as wrinkled.

TEM images of GO, ERGO, and TERGO powders are shown in Figures 6(a)–6(c). TEM micrographs confirm the formation of single crystalline structures, although it is also evident that the combination of more than one reduction route, specifically, electrochemical and thermal ones, led to obtain an effective removal of oxygen functional groups. During the reduction processes, the morphology is modified from paper-like graphene layers to wrinkled-type structures. Because the final reduced graphene oxide structure is highly dependent on the reduction strategy, it is reasonable to assume that combination of electrochemical and thermal methods reassembles the π -conjugated structure in order to change almost totally their hybridization to sp^2 [58].

3.2. PANI/ERGO Characterization

3.2.1. Raman Spectroscopy. The conductive behavior of polymers is achieved when the oxidizing agent interacts through the monomers with a lone pair of electrons; in this process, a free positive charge is formed (polarons) and is arisen from the coupling between electrons and phonons.

The PANI chains are formed from three basic segments: benzenoid, semiquinonoid, and quinonoid; all of them are associated to the leucoemeraldine, pernigraniline, and emeraldine states, respectively. Specifically, for its industrial interest, the polaronic and bipolaronic forms of PANI (emeraldine) have been studied by theoretical approaches [59–62].

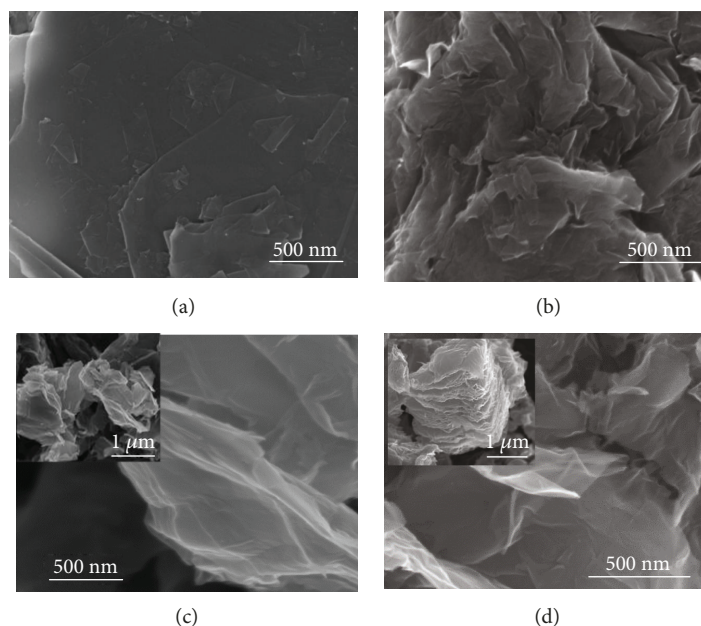


FIGURE 5: SEM micrographs of (a) graphite, (b) GO, (c) ERGO, and (d) TERGO.

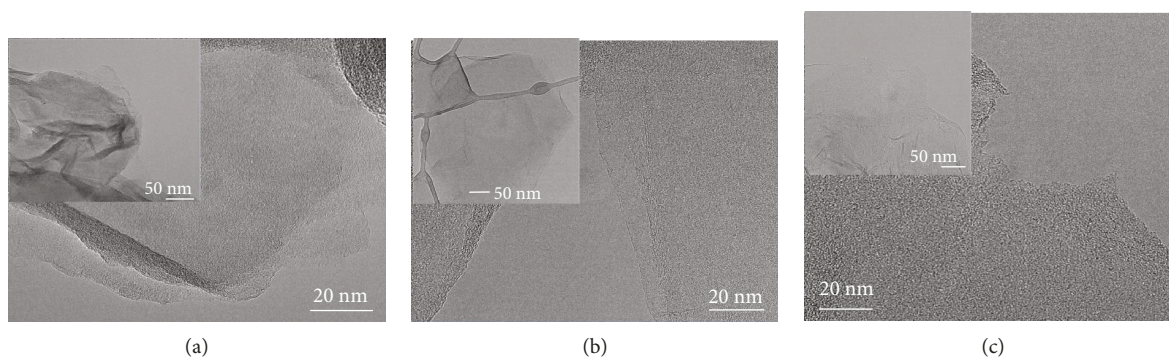


FIGURE 6: TEM micrographs of (a) GO, (b) ERGO, and (c) TERGO.

Raman spectroscopy was used to distinguish PANI polaronic states and evaluate the effect of adding different amounts of TERGO powders during the PANI polymerization. Raman spectra after adding 10, 20, and 30 wt% of TERGO powders are shown in Figures 7(a)–7(d).

Conductive PANI displays the $\nu(\text{C}=\text{N})$ stretching vibration of quinoid units and $\delta(\text{NH})$ deformation vibration associated to the semiquinoid structures located at $\sim 1490\text{ cm}^{-1}$ and 1508 cm^{-1} , respectively. Also, the $\nu(\text{C}\sim\text{N}^+)$ vibration of delocalized polaronic structures is located in the spectral range from 1324 to 1354 cm^{-1} .

In the spectra, a Raman shift at about 1335 cm^{-1} is observed and correlated with the deprotonation which is a result of polaron formation with small conjugation lengths. If a severe deprotonation occurs, a broad band is observed at 1380 cm^{-1} whereas its absence guarantees the protonation of the prepared PANI emeraldine base. Deprotonation in the hybrid materials is confirmed by the weak shoulders at 1506 cm^{-1} and 1583 cm^{-1} , both assigned to $\nu\text{C}=\text{N}$ and ν

$\text{C}=\text{C}$ modes of quinoid rings (Q band). The band of CH in-plane bending vibration at 1178 cm^{-1} corresponds to the semiquinoid ring (cation-radical segments). A typical sharp band at around 1375 cm^{-1} is missing in these spectra suggesting that there are no overoxidized segments, during the process. The bands at lower frequency, 421 and 515 cm^{-1} , emerge as a function of the used laser power. Finally, the centered band at 595 cm^{-1} can be associated to the cross-linked structure of phenazine-like rings.

PANI-TERGO composites showed similar Raman bands than that presented by neat PANI, but with reduction in the intensity, as observed for the peak ascribed to the polaron $\text{C}\sim\text{N}^+$ stretching mode at $\sim 1335\text{ cm}^{-1}$ (Figures 7(b)–7(d)). The reduction is even noticed since low TERGO amounts added to the polymeric matrix. The benzenoid ring deformations at 580 cm^{-1} and 813 cm^{-1} are also smooth after TERGO addition. It is well known that the main factors that affect intensity in Raman spectra of PANI polaron bonds included the following: (a) conjugation and quantity of π electrons in

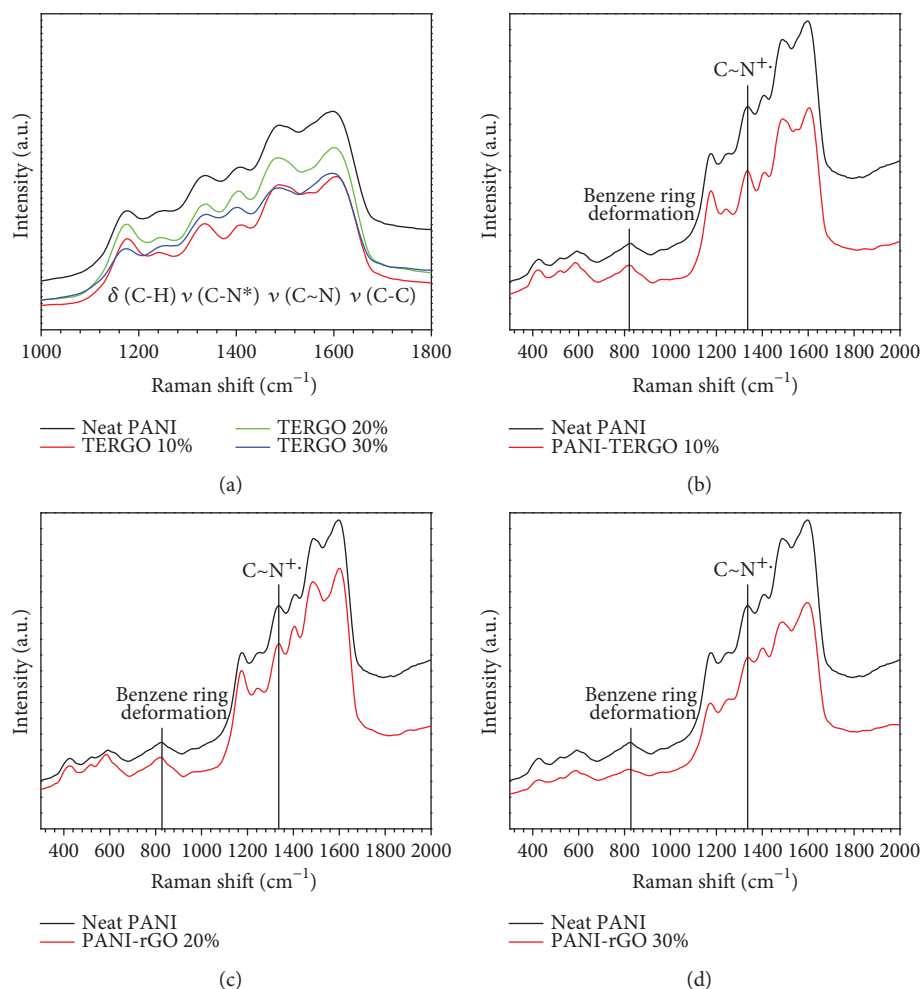


FIGURE 7: Raman spectra of (a) neat PANI and its comparison with the as-synthesized composites in the Raman shift range of 1000–1800 cm^{-1} , (b) PANI/ERGO (10 wt%), (c) PANI/ERGO (20 wt%), and (d) PANI/ERGO (30 wt%) and its comparison with pure PANI.

the chain, a high amount of π electrons provokes an increment in the intensity of Raman bands and a displacement to low Raman shift, (b) the chain protonation degree in the PANI (emeraldine) which is modified by the addition of TERGO powders, and (c) the ratio of symmetric (C~N⁺) and nonsymmetric (C~N⁺-C) polaronic bonds, i.e., chemical neighbor. Thus, under the experimental conditions, the presence of graphene powders clearly causes deterioration of the PANI polaron number; probably ascribed with a weak interaction between the PANI charge carrier and π electron density of TERGO.

3.2.2. UV-Vis Spectroscopy of PANI/TERGO Composites.

Figure 8 shows the UV-Vis spectra of the as-obtained composites and its comparison with pure PANI. Neat PANI have shown three main transitions, the first peak at around 360 nm is assigned to the $\pi - \pi^*$ transitions in benzenoid rings, the second at 450 nm, which is seen as a small transition, is also characteristic of polaronic transition (polaron π^*), and the last band appears at 820 nm and is attributable to the π polaron transition of quinoid rings through PANI chains [63, 64].

UV-vis spectra of hybrid composites show absorption band combination of both constituents. For example, the absorption band at 270 nm is associated with $n - \pi^*$ transitions generated during restoration of the electronic configuration (sp^2) and decreases with the TERGO amount. Differences in intensity are mainly due to conjugative effects of the chromophore unit (C=C and C-O bonds) that influences the $\pi - \pi^*$ transitions of graphitic structures [65]. An enlargement in the visible region (520–610 nm) showed an emerging band that shifts between 565 and 585 nm depending on TERGO quantity. It has been proposed that emeraldine absorption correlated with the $n - \pi^*$ excitation of the amine and imine segments appearing at 620 nm [66–68] but, it can be displaced at lower wavelengths in presence of reduction agent [69]. Thus, UV-Vis absorption features suggest that TERGO powders are acting as reducing agents shifting to low wavelength $n - \pi^*$ excitations.

3.2.3. FT-IR Measurements of PANI/TERGO Composites.

Figure 9 shows FTIR measurements of pure PANI and PANI/TERGO composites where it is seen that in general, after adding TERGO powders to neat PANI, the spectra

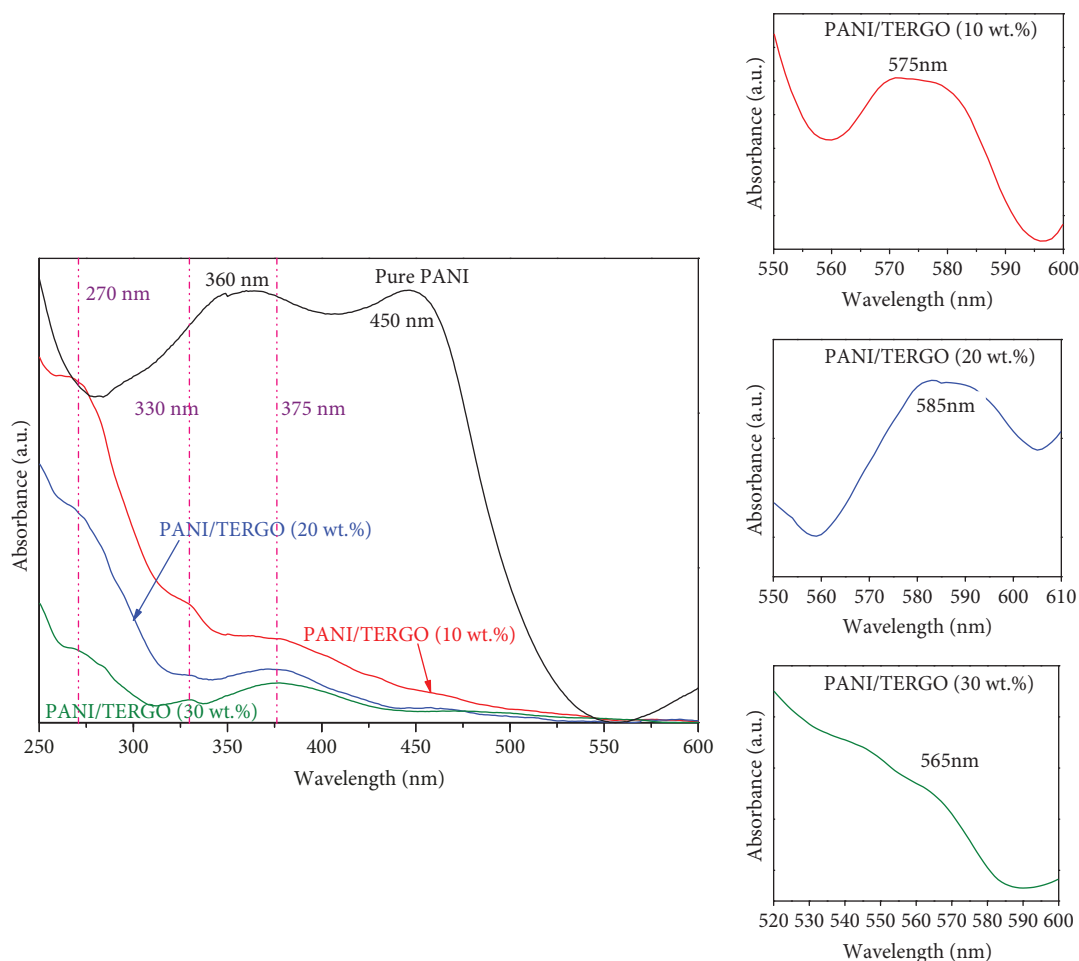


FIGURE 8: UV-Vis absorption spectra of PANI/TERGO composites with an amplification of the regions where new bands emerge.

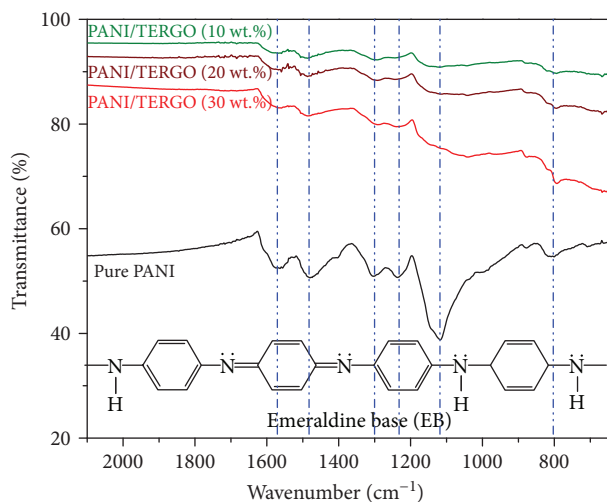


FIGURE 9: FT-IR spectra of PANI-TERGO composites and its comparison with pure PANI.

reduced the intensity of the main bands. Some displacements in the absorption bands provided evidence of composite formation. Specific features are analyzed as follows: FT-IR

spectra showed that the -OH stretching mode of TERGO and N-H stretching vibration of a secondary amine in the PANI backbone completely disappeared (see the inset of the emeraldine base structure, Figure 9). An important reduction in the intensity is observed in the quinonoid stretching ring (1559 cm^{-1}) and C-N^+ stretching on the polaron structure (1235 cm^{-1}) [70–74]. Thus, FT-IR spectra evidence that with the amount of TERGO powders, the transmittance is gradually reduced.

3.2.4. XRD of PANI/TERGO Composites. XRD spectra of PANI/TERGO composites with its corresponding deconvolution are shown in Figures 10(a)–10(e). Diffraction peaks at 9° , 14.6° , 20.5° , and 25.3° from (001), (011), (100), and (110) planes, respectively, matched well with the octahedral phase of PANI [69, 75, 76]. In the reflections from composites, any important change in positions was not detected. However, it was observed that the intensity and widening of the (110) plane decrease with TERGO quantity, reducing the crystallinity, crystallite size, or the weakened stacking along the specific direction of PANI [77]. To evaluate this modifications, XRD patterns were deconvoluted using a Lorentzian function and the fittings are shown in Figures 10(b)–10(e). PANI displays 61% of the crystalline

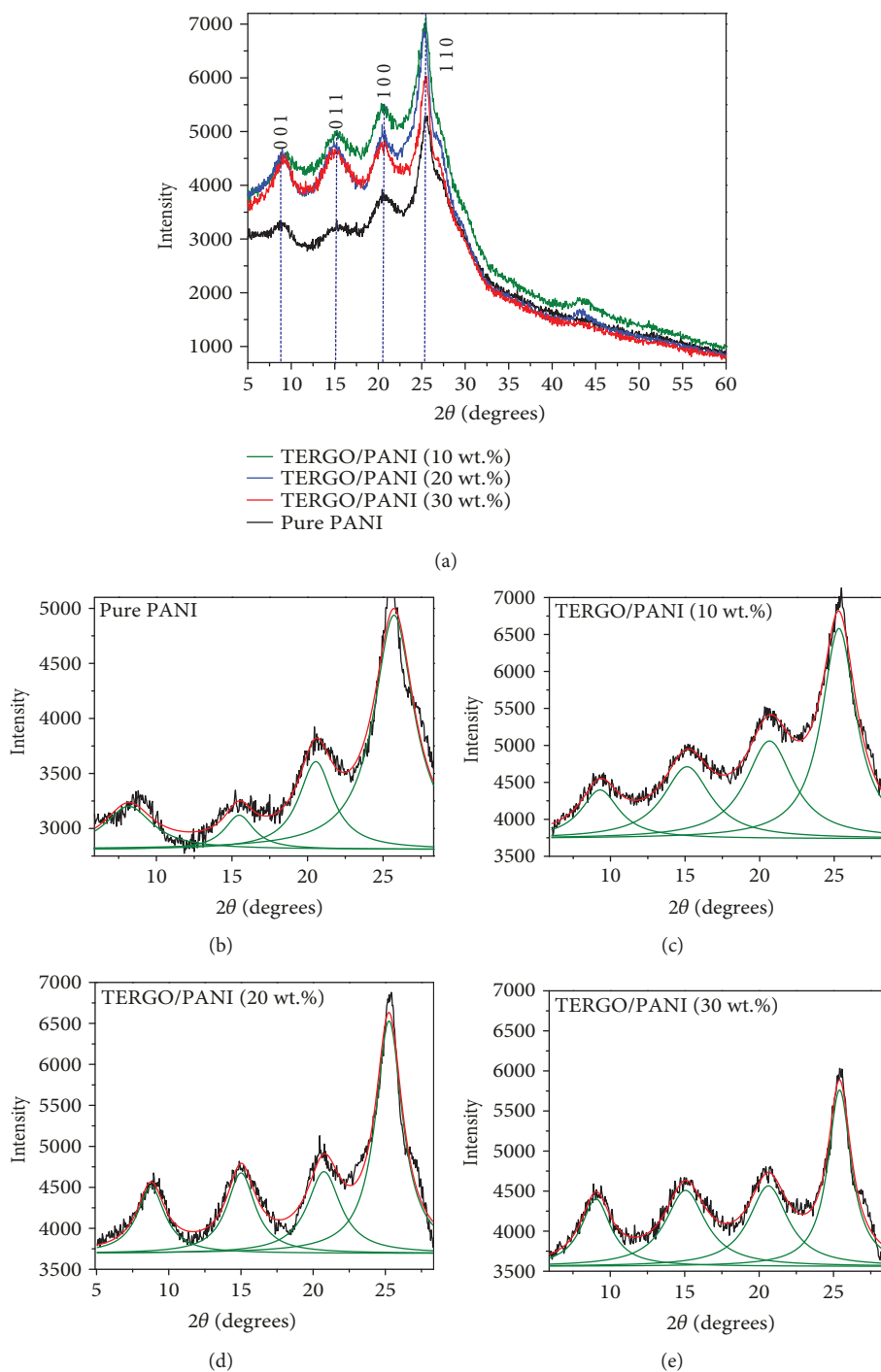


FIGURE 10: XRD of pure PANI and PANI/TERGO composites with its corresponding deconvolution.

phase and reduces up to 42%, 38%, and 36%, with TERGO addition of 10, 20, and 30 wt%, respectively.

3.2.5. Morphology of PANI/TERGO Composites. Figures 11(a)–11(f) show SEM micrographs of pure PANI and PANI/TERGO composites. Pure PANI shows long agglomerates formed by smaller semispherical particles; the average particle size is about 300 nm. Hybrid composites display a combined morphology between the PANI and TERGO

structures, suggesting a physical interaction between both morphologies.

The composites are composed of PANI-covering TERGO nanosheets. In agreement with previous reports, a high amount of graphene flakes occasionally breaks the film at higher thickness and characteristic wrinkled graphene nanosheet walls are evident [78]. Magnification of selected samples (Figures 12(a)–12(b)) confirms evolution of the morphologies dependent of the TERGO quantity.

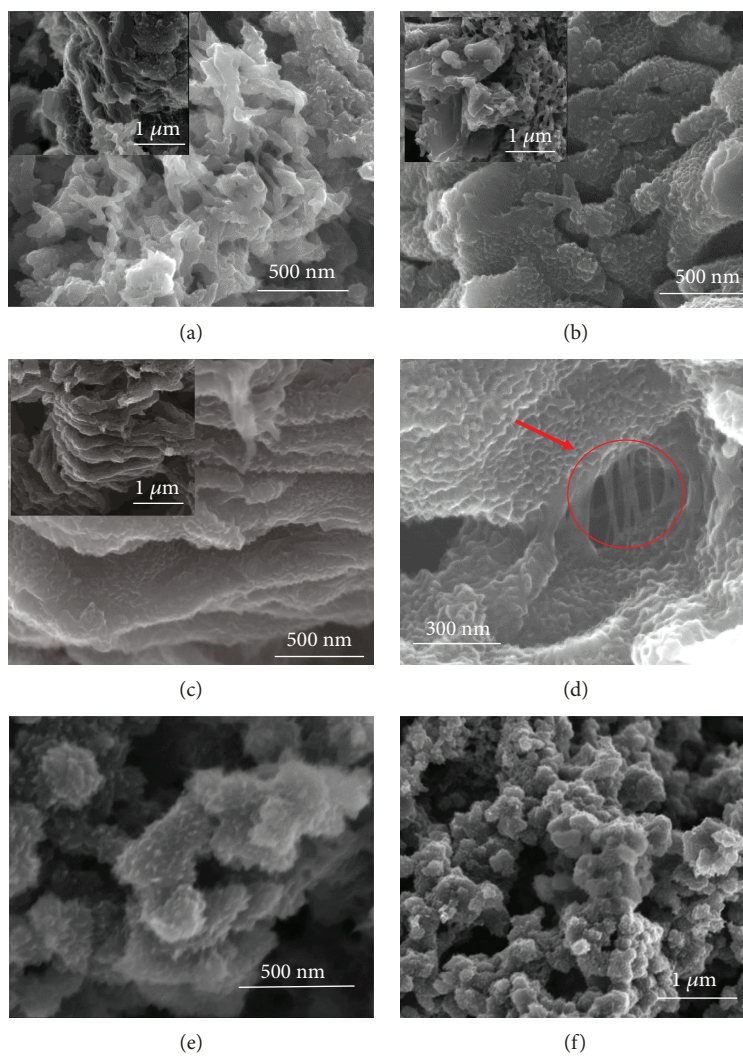


FIGURE 11: SEM images of PANI/TERGO composites at different magnifications with different amounts of reduced graphene oxide at (a) 10 wt%, (b) 20 wt%, (c, d) 30 wt%, and (e, f) pure PANI.

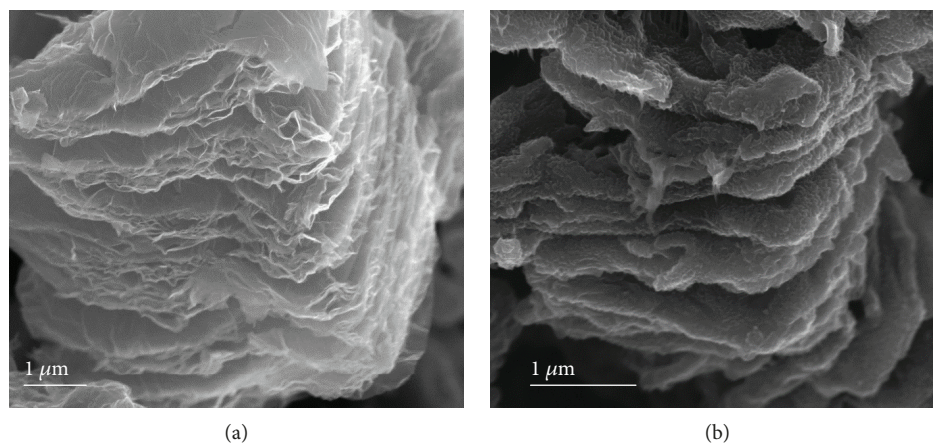


FIGURE 12: Comparison of SEM images of (a) TERGO and (b) PANI/TERGO (30 wt%).

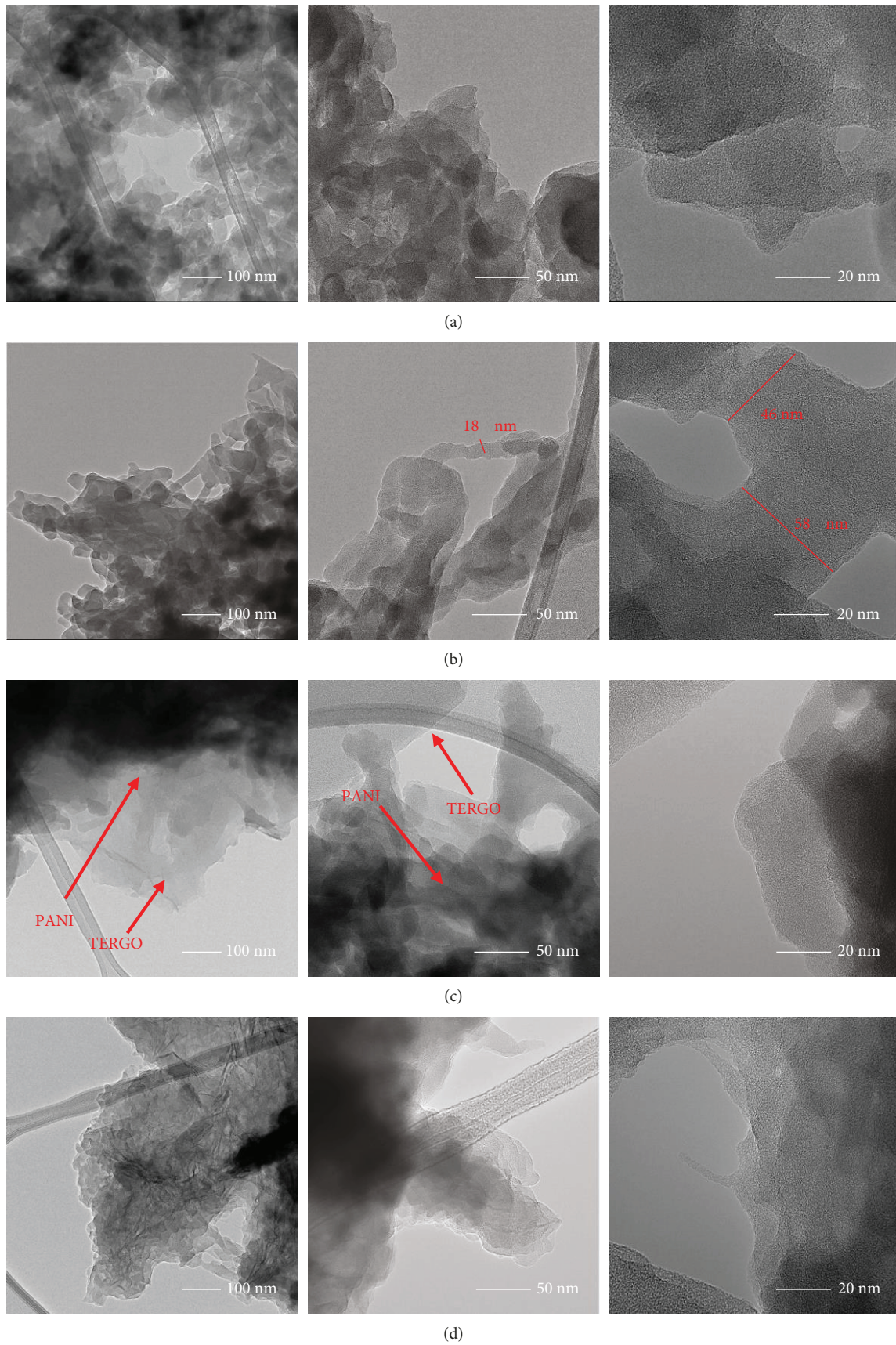


FIGURE 13: TEM micrographs of (a) pure PANI and PANI/TERGO composites at different magnifications with different amounts of reduced graphene oxide at (b) 10 wt%, (c) 20 wt%, and (d) 30 wt%.

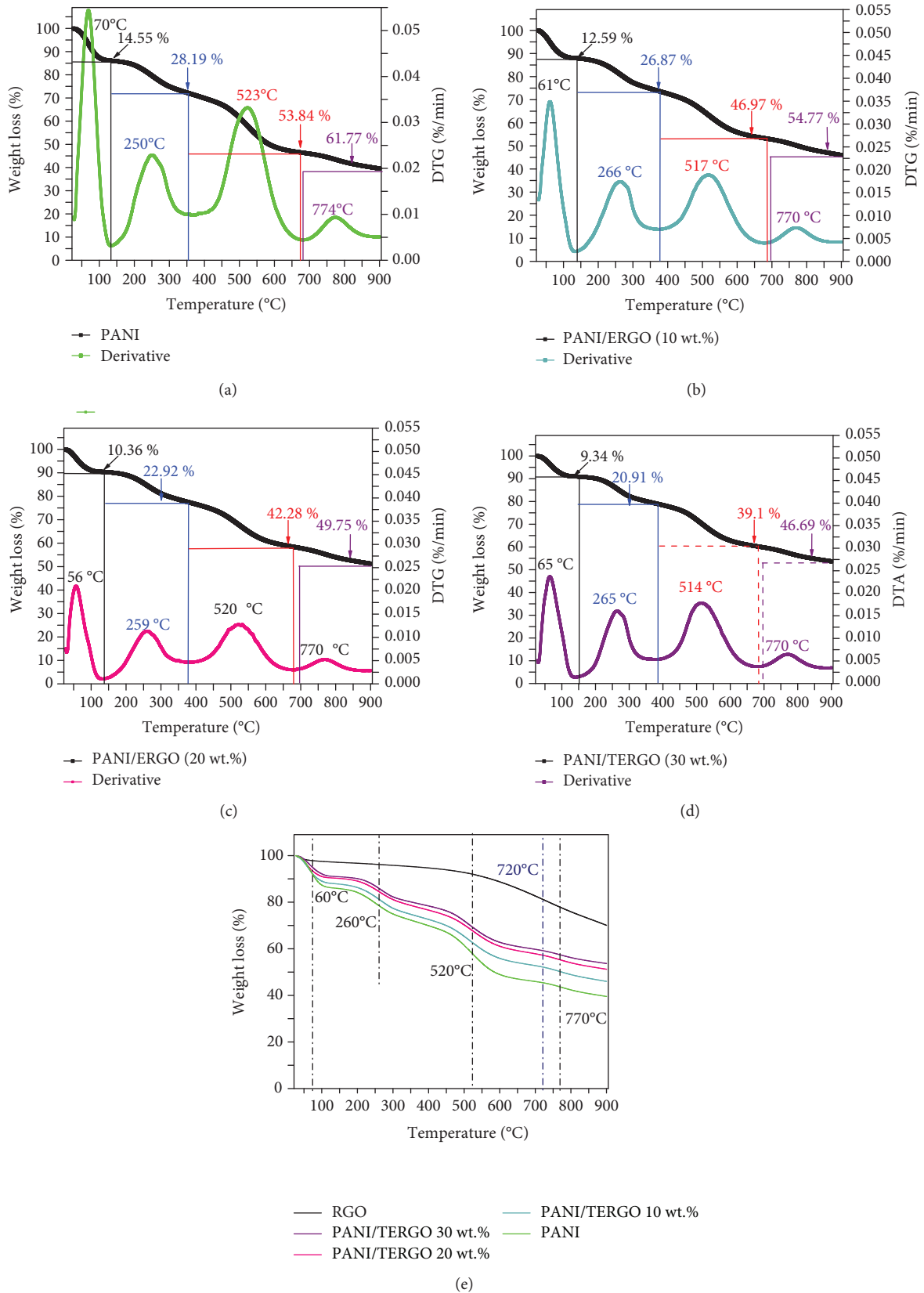


FIGURE 14: TGA/DTA thermograms of (a) PANI, (b) PANI/TERGO 10 wt%, (c) PANI/TERGO 20 wt%, (d) PANI/TERGO 30 wt%, and (e) TGA thermograms corresponding to PANI and PANI/TERGO composites and TERGO.

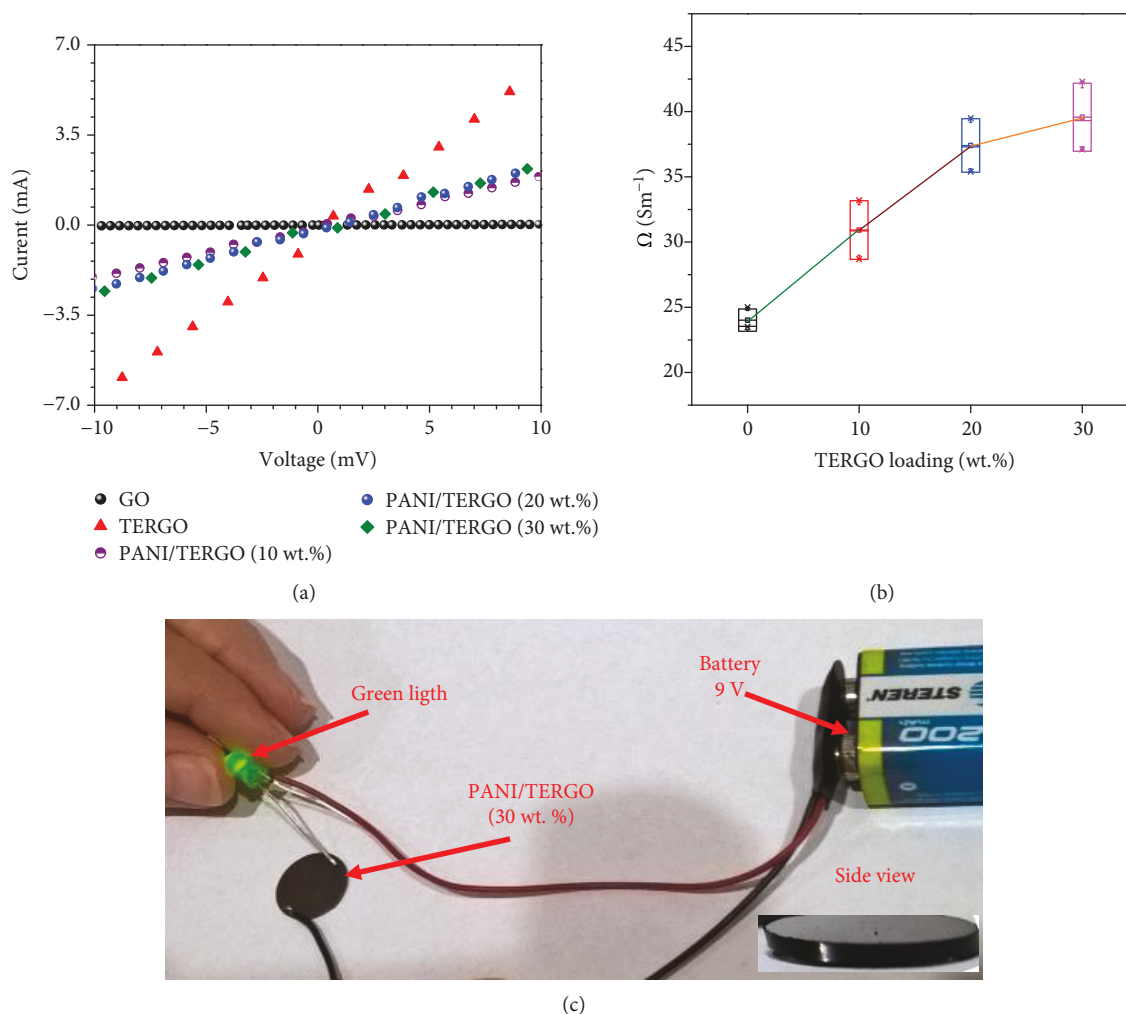


FIGURE 15: Electrical conductivity of the composites as a function of TERGO loading and the test of compressed films with 30 wt%.

TEM micrographs show the internal microstructure of composites, which change from a semispherical shape to extend sheets with the amount of TERGO powders (Figures 13(a)–13(d)) [79–81]. Evolution of the microstructure is consistent with SEM observations, i.e., PANI is sandwiched between ERGO layers.

3.2.6. DSC/TGA Analysis. Figures 14(a)–14(e) show the TGA curves and their derivatives for PANI and PANI/TERGO. The derivative curves indicate that the degradation of PANI occurs in four stages (Figure 14(a)). The first weight loss below 100°C (14.55%) is due to the absorbed moisture while the peak between 130 and 360°C (28.19% weight loss) is attributed to the dopant evaporation, i.e., to the water molecules that are attached and acted as a secondary bond of PANI. Another intermediate is between 400 and 680°C (53.84%), which is correlated to the carbonization of the PANI backbone. Finally, in the temperature range of 680 – 900°C (61.77%), the subsequent burning of carbon is obtained. There is an important change in the thermal stability of PANI with TERGO incorporation (Figures 14(b)–14(d)). Dependent of TERGO amounts,

the weight loss decreases in each stage. Values of weight loss % at the final stage were as follows: 54.77% (10 wt%), 49.7% (20 wt%), and 46.69% (30 wt%). Weight loss reduction is a direct consequence of the thermal stability obtained by the physical interaction between composite constituents (Figure 14(e)).

3.3. Electrical Performance. Figures 15(a)–15(c) display the electrical properties of PANI, GO, and TERGO with different amounts added to the polymeric matrix (10, 20, and 30 wt%). In the plot, the reciprocal of the slope represents the electrical resistance of the compressed films (Figure 15(a)). The insulator behavior of GO is clearly observed in the figure. As expected, a higher difference was found in the electrical conductivity of GO and TERGO powders with values of $\sim 0.41 \text{ S/m}$ and $\sim 100 \text{ S/m}$, respectively (Figure 15(b)). In good agreement with previous reports, the pure PANI exhibit an electrical conductivity of $\sim 24 \text{ S/m}$; surprisingly, when TERGO was added to the PANI matrix, the conductivity of composites only increases in the range of 30 – 39 Sm^{-1} , independently of the TERGO quantity, i.e., the electrical conductivity values of hybrid composites remain

close to pure PANI and quite low in comparison with TERGO particles. Recent investigations have demonstrated that an improvement in the electrical conductivity of hybrid composites is correlated with the high aspect ratio of the carbon microstructure (carbon hexagonal lattice) and the interaction with the polymeric matrix, where the adatoms act as bridges for the electron transport which in turn favored the electrical conductivity. Thus, the prepared PANI-TERGO composites exhibit a poor increment in the electrical conductivity that is correlated with the observed morphology. TERGO plates coated with PANI do not influence positively the $\pi - \pi^*$ transition of PANI because TERGO do not present a total planar structure of graphene sheets. The planar structure is required to increase the contact area between PANI and TERGO and constructed a conductive network with a higher electron transfer rate (low resistance) [78]. The rough TERGO surface conditioned the homogeneous nucleation of a large amount of polymer (PANI) reducing the area to move the electrical charge.

4. Conclusions

TERGO films were synthesized by combining modified Hummer's process followed by two reduction methods (electrochemical and thermal processes). The electrical properties of PANI/TERGO composites were analyzed in terms of interaction type, TERGO amount, and morphology. From the above results, the following conclusions can be identified.

- (i) Combining suitable conditions of the electrochemical and thermal methodologies, it can effectively induce surface defects in graphene oxide structures. The defects were produced by typical pathways such as eliminating oxygen groups, improving the $\pi - \pi$ stacking, and provoking strong interactions between TERGO sheets
- (ii) The XRD peak at 24.5° with an interlayer space of 3.62 \AA confirms a poor ordering in the stacking direction
- (iii) The addition of TERGO layers to PANI provokes a reduction in the intensity in different Raman shifts because it affects partially the PANI polaron number. The interaction occurs between the PANI charge carrier and TERGO π electron density
- (iv) The reduction intensity was also observed in FT-IR measurements, specifically at 1559 cm^{-1} and 1235 cm^{-1} , which corresponds to the quinonoid stretching ring and to the C-N⁺ stretching in the polaron structure
- (v) PANI-TERGO composites provide a mixed morphology between pure PANI and TERGO powders, but this influences negatively the $\pi - \pi^*$ transition of PANI because TERGO do not present a total planar structure of graphene sheets. Thus, a rough TERGO surface conditioned the homogeneous nucleation of a large amount of polymer (PANI) reducing the area to move the electrical charge.

The maximum electrical conductivity was obtained with 30 wt% of TERGO being added to the PANI matrix.

Data Availability

The data used to support the findings of this study are available from the corresponding author upon request.

Conflicts of Interest

The authors declare that they have no conflicts of interest.

Acknowledgments

The authors are grateful for the financial support provided by the Consejo Nacional de Ciencia y Tecnología Research Fellowship-IPN-CICATA Altamira agreement, 2014-1905, and CONACyT CB2015-252181 projects and Instituto Politécnico Nacional through the SIP2018-0496 and SIP2018-1171 projects as well as SNI-CONACyT. Thanks are due to M. E. Adela E. Rodríguez-Salazar for her technical support during the revision of the manuscript.

Supplementary Materials

Figure S1: TERGO micrographs of the restored $\pi - \pi^*$ network where it is possible to observe the transparent graphene layer observed at (a) 100 nm and (b) 50 nm. Figure S2: TGA of graphene oxide, ERGO, and TERGO where weight loss is observable. (*Supplementary Materials*)

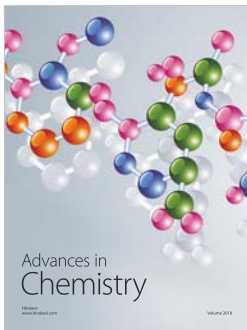
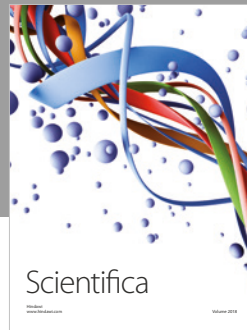
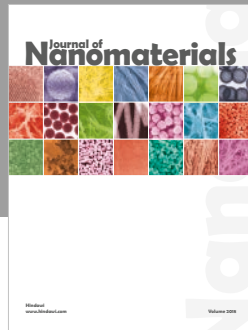
References

- [1] L. L. Zhang and X. S. Zhao, "Carbon-based materials as supercapacitor electrodes," *Chemical Society Reviews*, vol. 38, no. 9, pp. 2520–2531, 2009.
- [2] N. Song, W. Wang, Y. Wu, D. Xiao, and Y. Zhao, "Fabrication of highly ordered polyaniline nanocone on pristine graphene for high-performance supercapacitor electrodes," *Journal of Physics and Chemistry of Solids*, vol. 115, pp. 148–155, 2018.
- [3] G. Wang, X. Liua, S. Liua et al., "The electrocapacitive properties of polyaniline/VXC-72 composite electrodes," *Colloids and Surfaces A: Physicochemical and Engineering Aspects*, vol. 540, pp. 98–105, 2018.
- [4] M. M. P. Parel, A. V. Gillado, and M. U. Herrera, "Morphology and electrical conductivity of polyaniline coating on acetate film," *Surfaces and Interfaces*, vol. 10, pp. 74–77, 2018.
- [5] Y. Shi, Z. Li, J. Shi et al., "Titanium dioxide-polyaniline/silk fibroin microfiber sensor for pork freshness evaluation," *Sensors and Actuators, B: Chemical*, vol. 260, pp. 465–474, 2018.
- [6] Y. Zhao, Z. Zhang, L. Yu, and T. Jiang, "Hydrophobic polystyrene/electro-spun polyaniline coatings for corrosion protection," *Synthetic Metals*, vol. 234, pp. 166–174, 2017.
- [7] Y. Zoua, J. Duan, Z. Qi, Y. Wang, S. Dong, and Z. Li, "Nonfilling polyaniline coating of sulfur/acetylene black for high-performance lithium sulfur batteries," *Journal of Electroanalytical Chemistry*, vol. 811, pp. 46–52, 2018.

- [8] B. Wang, J. Tang, and F. Wang, "Electrochemical polymerization of aniline," *Synthetic Metals*, vol. 18, no. 1-3, pp. 323–328, 1987.
- [9] G. G. Wallace, P. R. Teasdale, G. M. Spinks, and L. A. P. Kane-Maguire, *Conductive Electroactive Polymers: Intelligent Polymer Systems*, CRC press, Taylor & Francis Group, Boca Raton, FL, USA, 3rd edition, 2008.
- [10] N. R. Tanguy, M. Thompson, and N. Yan, "A review on advances in application of polyaniline for ammonia detection," *Sensors and Actuators B: Chemical*, vol. 257, pp. 1044–1064, 2018.
- [11] S. Bilal, M. Fahim, I. Firdous, and A. A. Shah, "Insight into capacitive performance of polyaniline/graphene oxide composites with ecofriendly binder," *Applied Surface Science*, vol. 435, pp. 91–101, 2018.
- [12] K. S. Novoselov, A. K. Geim, S. V. Morozov et al., "Electric field effect in atomically thin carbon films," *Science*, vol. 306, no. 5696, pp. 666–669, 2004.
- [13] A. K. Geim and K. S. Novoselov, "The rise of graphene," *Nature Materials*, vol. 6, no. 3, pp. 183–191, 2007.
- [14] C. Lee, X. Wei, J. W. Kysar, and J. Hone, "Measurement of the elastic properties and intrinsic strength of monolayer graphene," *Science*, vol. 321, no. 5887, pp. 385–388, 2008.
- [15] C. Yang, L. Zhang, N. Hu et al., "Rational design of sandwiched polyaniline nanotube/layered graphene/polyaniline nanotube papers for high-volumetric supercapacitors," *Chemical Engineering Journal*, vol. 309, pp. 89–97, 2017.
- [16] H. P. Cong, X. C. Ren, P. Wang, and S. H. Yu, "Flexible graphene-polyaniline composite paper for high-performance supercapacitor," *Energy & Environmental Science*, vol. 6, no. 4, pp. 1185–1191, 2013.
- [17] C. Gaynera and K. K. Kar, "Recent advances in thermoelectric material," *Progress in Materials Science*, vol. 83, pp. 330–382, 2016.
- [18] F. D. Rosi, "Thermoelectricity and thermoelectric power generation," *Solid State Electronics*, vol. 11, no. 9, pp. 833–868, 1968.
- [19] R. P. Chasmar and R. Stratton, "The thermoelectric figure of merit and its relation to thermoelectric generators," *Journal of Electronics and Control*, vol. 7, no. 1, pp. 52–72, 1959.
- [20] H. J. Goldsmith, "Introduction to thermoelectricity," in *Springer Series in Materials Science*, R. Hull, J. Parisi, R. M. Osgood Jr., and H. Warlimont, Eds., vol. 121, Springer, Berlin, Heidelberg, 2010.
- [21] O. T. Ikkala, L. O. Pietila, L. Ahjopalo, H. Osterholm, and P. J. Passiniemi, "On the molecular recognition and associations between electrically conducting polyaniline and solvents," *The Journal of Chemical Physics*, vol. 103, no. 22, pp. 9855–9863, 1995.
- [22] L. Jun, L. M. Zhang, L. He, and X. F. Tang, "Synthesis and thermoelectric properties of polyaniline," *Journal of Wuhan University of Technology-Mater. Sci. Ed*, vol. 18, no. 3, pp. 53–55, 2003.
- [23] S. Bhadra, D. Khastgir, N. K. Singha, and J. H. Lee, "Progress in preparation, processing and applications of polyaniline," *Progress in Polymer Science*, vol. 34, no. 8, pp. 783–810, 2009.
- [24] J. J. Li, X. F. Tang, H. Li, Y. G. Yan, and Q. J. Zhang, "Synthesis and thermoelectric properties of hydrochloric acid doped polyaniline," *Synthetic Metals*, vol. 160, no. 11-12, pp. 1153–1158, 2010.
- [25] W. S. Hummers and R. E. Offeman, "Preparation of graphitic oxide," *Journal of the American Chemical Society*, vol. 80, no. 6, article 1339, 1958.
- [26] M. S. Seehra, V. Narang, U. K. Geddam, and A. B. Stefaniak, "Correlation between X-ray diffraction and Raman spectra of 16 commercial graphene-based materials and their resulting classification," *Carbon*, vol. 111, pp. 380–385, 2017.
- [27] A. Das, B. Chakraborty, and A. K. Sood, "Raman spectroscopy of graphene on different substrates and influence of defects," *Bulletin of Materials Science*, vol. 31, no. 3, pp. 579–584, 2008.
- [28] J. W. Moore and C. L. Stanitski, *Chemistry: the Molecular Science*, Cengage learning, Stamford, 5th edition, 2015.
- [29] J. M. Munuera, J. I. Paredes, M. Enterría et al., "Electrochemical exfoliation of graphite in aqueous sodium halide electrolytes toward low oxygen content graphene for energy and environmental applications," *ACS Applied Materials & Interfaces*, vol. 9, no. 28, pp. 24085–24099, 2017.
- [30] S. Abdolhosseinzadeh, H. Asgharzadeh, and H. S. P. Kim, "Fast and fully-scalable synthesis of reduced graphene oxide," *Scientific Reports*, vol. 5, no. 1, article 10160, 2015.
- [31] T. K. Gupta, B. P. Singh, R. B. Mathur, and S. R. Dhakate, "Multi-walled carbon nanotube-graphene-polyaniline multi-phase nanocomposite with superior electromagnetic shielding effectiveness," *Nanoscale*, vol. 6, no. 2, pp. 842–851, 2014.
- [32] M. Balabajew, H. Reinhardt, N. Bock et al., "In-situ Raman study of the intercalation of Bis(trifluoromethylsulfonyl)imid ions into graphite inside a dual-ion cell," *Electrochimica Acta*, vol. 211, pp. 679–688, 2016.
- [33] W.-J. Ong, L.-L. Tan, S.-P. Chai, S.-T. Yong, and A. R. Mohamed, "Surface charge modification via protonation of graphitic carbon nitride (g-C₃N₄) for electrostatic self-assembly construction of 2D/2D reduced graphene oxide (rGO)/g-C₃N₄ nanostructures toward enhanced photocatalytic reduction of carbon dioxide to methane," *Nano Energy*, vol. 13, pp. 757–770, 2015.
- [34] A. Goñi, A. Iturrondobeitia, I. Gil de Muro, L. Lezama, and T. Rojo, "Na_{2.5}Fe_{1.75}(SO₄)₃/Ketjen/rGO: an advanced cathode composite for sodium ion batteries," *Journal of Power Sources*, vol. 369, pp. 95–102, 2017.
- [35] A. Kaniyoor and S. Ramaprabhu, "A Raman spectroscopic investigation of graphite oxide derived graphene," *AIP Advances*, vol. 2, no. 3, article 032183, pp. 1–13, 2012.
- [36] L. G. Cançado, A. Jorio, E. H. M. Ferreira et al., "Quantifying defects in graphene via Raman spectroscopy at different excitation energies," *Nano Letters*, vol. 11, no. 8, pp. 3190–3196, 2011.
- [37] S. Lee, S. Lim, E. Lim, and K. K. Lee, "Synthesis of aqueous dispersion of graphenes via reduction of graphite oxide in the solution of conductive polymer," *Journal of Physics and Chemistry of Solids*, vol. 71, no. 4, pp. 483–486, 2010.
- [38] T. Fan, W. Zeng, W. Tang et al., "Controllable size-selective method to prepare graphene quantum dots from graphene oxide," *Nanoscale Research Letters*, vol. 10, no. 1, p. 55, 2015.
- [39] B. Manoj, A. M. Raj, and G. T. Chirayil, "Tunable direct band gap photoluminescent organic semiconducting nanoparticles from lignite," *Scientific Reports*, vol. 7, no. 1, article 18012, 2017.
- [40] G. Wang, X. Sun, C. Liu, and J. Lian, "Tailoring oxidation degrees of graphene oxide by simple chemical reactions," *Applied Physics Letters*, vol. 99, no. 5, article 053114, 2011.

- [41] C. Petit, M. Seredych, and T. J. Bandosz, "Revisiting the chemistry of graphite oxides and its effect on ammonia adsorption," *Journal of Materials Chemistry*, vol. 19, no. 48, pp. 9176–9185, 2009.
- [42] S. Drewniak, R. Muzyka, A. Stolarczyk, T. Pustelny, M. Kotyczka-Morańska, and M. Setkiewicz, "Studies of reduced graphene oxide and graphite oxide in the aspect of their possible application in gas sensors," *Sensors*, vol. 16, no. 1, p. 103, 2016.
- [43] W. S. Chong, W. C. Lai, and S. B. A. Hamid, "Controllable electrochemical synthesis of reduced graphene oxide thin-film constructed as efficient photoanode in dye-sensitized solar cells," *Materials*, vol. 9, no. 2, p. 69, 2016.
- [44] L. Shahriary and A. A. Athawale, "Graphene oxide synthesized by using modified hummers approach," *International Journal of Renewable Energy and Environmental Engineering*, vol. 2, pp. 58–63, 2014.
- [45] J. Malig, J. M. Englert, A. Hirsch, and D. Guldi, "Wet chemistry of graphene," *Interface magazine*, vol. 20, no. 1, pp. 53–56, 2011.
- [46] K. L. S. Castro, S. M. Oliveira, R. V. Curti et al., "Electrochemical response of glassy carbon electrodes modified using graphene sheets of different sizes," *International Journal of Electrochemical Science*, vol. 13, pp. 71–87, 2018.
- [47] N. Popova, "Crystallographic analysis of graphite by X-ray diffraction," *Coke and Chemistry*, vol. 60, no. 9, pp. 361–365, 2017.
- [48] B. S. Yilbas, A. Ibrahim, H. Ali, M. Khaled, and T. Laoui, "Hydrophobic and optical characteristics of graphene and graphene oxide films transferred onto functionalized silica particles deposited glass surface," *Applied Surface Science*, vol. 442, pp. 213–223, 2018.
- [49] S. S. Alam, N. Sharma, and L. Kumar, "Synthesis of graphene oxide (GO) by modified hummers method and its thermal reduction to obtain reduced graphene oxide (rGO)," *Graphene*, vol. 6, no. 1, pp. 1–18, 2017.
- [50] K. Karami and N. S. Mousavi, "A palladium complex immobilized onto a magnetic GO-MnFe₂O₄ surface as an effective and recyclable catalyst for the reduction of p-nitrophenol," *Dalton Transactions*, vol. 47, no. 12, pp. 4175–4182, 2018.
- [51] L.-Q. Xie, Y.-H. Zhang, F. Gao et al., "A highly sensitive dopamine sensor based on a polyaniline/reduced graphene oxide/Nafion nanocomposite," *Chinese Chemical Letters*, vol. 28, no. 1, pp. 41–48, 2017.
- [52] R. Thekkayil, H. John, and P. Gopinath, "Grafting of self assembled polyaniline nanorods on reduced graphene oxide for nonlinear optical application," *Synthetic Metals*, vol. 185–186, pp. 38–44, 2013.
- [53] L. Y. Meng and S. J. Park, "Preparation and characterization of reduced graphene nanosheets via pre-exfoliation of graphite flakes," *Bulletin of the Korean Chemical Society*, vol. 33, no. 1, pp. 209–214, 2012.
- [54] J. A. Rather, E. A. Khudaish, A. Munam, A. Qurashi, and P. Kannan, "Electrochemically reduced fullerene-graphene oxide interface for swift detection of Parkinsons disease biomarkers," *Sensors and Actuators B: Chemical*, vol. 237, pp. 672–684, 2016.
- [55] S. Palanisamy, B. Thirumalraj, S. M. Chen, Y. T. Wang, V. Velusamy, and S. K. Ramaraj, "A facile electrochemical preparation of reduced graphene oxide@polydopamine composite: a novel electrochemical sensing platform for amperometric detection of chlorpromazine," *Scientific Reports*, vol. 6, no. 1, 2016.
- [56] L. Wang, Q. Yao, H. Bi, F. Huang, Q. Wang, and L. Chen, "PANI/graphene nanocomposite films with high thermoelectric properties by enhanced molecular ordering," *Journal of Materials Chemistry A*, vol. 3, no. 13, pp. 7086–7092, 2012.
- [57] S. K. Deng and V. Berry, "Wrinkled, rippled and crumpled graphene: an overview of formation mechanism, electronic properties, and applications," *Materials Today*, vol. 19, no. 4, pp. 197–212, 2016.
- [58] A. B. López-Oyama, M. A. Domínguez-Crespo, A. M. Torres-Huerta, E. Onofre-Bustamante, R. Gámez-Corrales, and N. Cayetano-Castro, "Electrochemical alternative to obtain reduced graphene oxide by pulse potential: effect of synthesis parameters and study of corrosion properties," *Diamond and Related Materials*, vol. 88, pp. 167–188, 2018.
- [59] M. Canales, J. Torras, G. Fabregat, A. Meneguzzi, and C. Aleman, "Polyaniline emeraldine salt in the amorphous solid state: polaron versus bipolaron," *The Journal of Physical Chemistry. B*, vol. 118, no. 39, pp. 11552–11562, 2014.
- [60] S. Stafstrom, J. L. Bredas, A. J. Epstein et al., "POLARON lattice in highly conducting polyaniline - theoretical and optical studies," *Physical Review Letters*, vol. 59, no. 13, pp. 1464–1467, 1987.
- [61] N. Gospodinova, S. Dorey, A. Ivanova, H. Zhekova, and A. Tadjer, "Evidence for generation of delocalized polarons in conducting polyaniline: a Raman scattering spectroscopy approach," *International Journal of Polymer Analysis and Characterization*, vol. 12, no. 3, pp. 251–271, 2007.
- [62] M. Aymen, S. Sami, S. Ahmed, G. Fethi, and B. M. Abdellatif, "Correlation between Raman spectroscopy and electrical conductivity of graphite/polyaniline composites reacted with hydrogen peroxide," *Journal of Physics D: Applied Physics*, vol. 46, no. 33, article 335103, 2013.
- [63] T. Abdiryim, Z. Xiao-Gang, and R. Jamal, "Comparative studies of solid-state synthesized polyaniline doped with inorganic acids," *Materials Chemistry and Physics*, vol. 90, no. 2–3, pp. 367–372, 2005.
- [64] S. Shahabuddin, N. M. Sarih, F. H. Ismail, M. M. Shahid, and N. M. Huang, "Synthesis of chitosan grafted-polyaniline/Co₃O₄ nanocube nanocomposites and their photocatalytic activity toward methylene blue dye degradation," *RSC Advances*, vol. 5, no. 102, pp. 83857–83867, 2015.
- [65] Q. Lai, S. Zhu, X. Luo, M. Zou, and S. Huang, "Ultraviolet-visible spectroscopy of graphene oxides," *AIP Advances*, vol. 2, no. 3, article 032146, 2012.
- [66] M. X. Wan and J. P. Yang, "Mechanism of proton doping in polyaniline," *Journal of Applied Polymer Science*, vol. 55, no. 3, pp. 399–405, 1995.
- [67] Y. H. Kim, C. Foster, J. Chiang, and A. J. Heeger, "Localized charged excitations in polyaniline: infrared photoexcitation and protonation studies," *Synthetic Metals*, vol. 29, no. 1, pp. 285–290, 1989.
- [68] P. S. Rao, J. Anand, S. Palaniappan, and D. N. Sathyanarayana, "Effect of sulphuric acid on the properties of polyaniline-HCl salt and its base," *European Polymer Journal*, vol. 36, no. 5, pp. 915–921, 2000.
- [69] P. Kar and A. Choudhury, "Carboxylic acid functionalized multi-walled carbon nanotube doped polyaniline for

- chloroform sensors,” *Sensors and Actuators B: Chemical*, vol. 183, pp. 25–33, 2013.
- [70] H. Baniasadi, S. A. A. Ramazani, S. Mashayekhan, and F. Ghaderinezhad, “Preparation of conductive polyaniline/graphene nanocomposites via in situ emulsion polymerization and product characterization,” *Synthetic Metals*, vol. 196, pp. 199–205, 2014.
- [71] E. M. Elnaggar, K. I. Kabel, A. A. Farag, and A. G. Al-Gamal, “Comparative study on doping of polyaniline with graphene and multi-walled carbon nanotubes,” *Journal of Nanostructure in Chemistry*, vol. 7, no. 1, pp. 75–83, 2017.
- [72] P. Modak, S. B. Kondawar, and D. V. Nandanwar, “Synthesis and characterization of conducting polyaniline/graphene nanocomposites for electromagnetic interference shielding,” *Procedia Materials Science*, vol. 10, no. 10, pp. 588–594, 2015.
- [73] Y. F. Zhang, J. Liu, Y. H. Zhang, and Y. P. Duan, “Facile synthesis of hierarchical nanocomposites of aligned polyaniline nanorods on reduced graphene oxide nanosheets for microwave absorbing materials,” *RSC Advances*, vol. 7, no. 85, pp. 54031–54038, 2017.
- [74] B. D. Ossoinon and D. Belanger, “Synthesis and characterization of sulfophenyl-functionalized reduced graphene oxide sheets,” *RSC Advances*, vol. 7, no. 44, pp. 27224–27234, 2017.
- [75] Z. M. Zhang, J. Sui, L. J. Zhang, M. X. Wan, Y. Wei, and L. M. Yu, “Synthesis of polyaniline with a hollow, octahedral morphology by using a cuprous oxide template,” *Advanced Materials*, vol. 17, no. 23, pp. 2854–2857, 2005.
- [76] Z.-J. Gu and Q. Shen, “Synthesis, characterization and comparison of polyaniline 1D-structure controlled by poly(l-lactide) and poly(d-lactide),” *Superlattices and Microstructures*, vol. 89, pp. 53–58, 2016.
- [77] N. L. Chen, Y. P. Ren, P. P. Kong, L. Tan, H. X. Feng, and Y. C. Luo, “In situ one-pot preparation of reduced graphene oxide/polyaniline composite for high-performance electrochemical capacitors,” *Applied Surface Science*, vol. 392, pp. 71–79, 2017.
- [78] S. Gupta and C. Price, “Investigating graphene/conducting polymer hybrid layered composites as pseudocapacitors: interplay of heterogeneous electron transfer, electric double layers and mechanical stability,” *Composites Part B: Engineering*, vol. 105, pp. 46–59, 2016.
- [79] S. Gupta, B. McDonald, S. B. Carrizosa, and C. Price, “Microstructure, residual stress, and intermolecular force distribution maps of graphene/polymer hybrid composites: nanoscale morphology-promoted synergistic effects,” *Composites Part B Engineering*, vol. 92, pp. 175–192, 2016.
- [80] X. Q. Jiang, S. Setodoi, S. Fukumoto et al., “An easy one-step electrosynthesis of graphene/polyaniline composites and electrochemical capacitor,” *Carbon*, vol. 67, pp. 662–672, 2014.
- [81] M. Shabani-Nooshabadi and F. Zahedi, “Electrochemical reduced graphene oxide-polyaniline as effective nanocomposite film for high-performance supercapacitor applications,” *Electrochimica Acta*, vol. 245, pp. 575–586, 2017.



Hindawi
Submit your manuscripts at
www.hindawi.com

